doi:10.15625/2525-2518/20703



Improved efficiency of bulk heterojunction polymer solar cells by omitting electron transport layer: a SCAPS 1D simulation study

Ramabadran C. D.^{1,3}, Dhanya N. P.^{2,*}, Sudheer K. S.^{1,*}

¹Department of Physics, Opto-electronic Device Simulation Research Lab, Christ College [Autonomous], Irinjalakuda, Thrissur, 680125, Kerala, India

² Department of Physics, KKTM Govt. College, Pullut, Thrissur, 680663, University of Calicut, Kerala, India

³Department of Physics, Government College, Chittur, Palakkad, 678104, University of Calicut, Kerala, India

> *Emails: 1.ramabadrancd@christcollegeijk.edu.in, <u>2. dhanyaajan@gmail.com</u>, 3. sudheersebastian@christcollegeijk.edu.in

Received: 1 May 2024; Accepted for publication: 16 September 2024

Abstract. This paper examines the function of bulk heterojunction polymer solar cells (BHJPSCs) in the realm of photovoltaics. Specifically, the performance of a BHJPSC setup eliminating the electron transport layer (ETL) is investigated. With the aid of SCAPS 1D software, simulation studies are done to evaluate the effectiveness of this innovative approach. Initially, the program is standardized by replicating a key experimental study that used P3HT:IC₆₀BA as the active layer, producing results consistent with actual observations. The solar cell structure ITO/PEDOT:PSS/P3HT:IC₆₀BA/ZnO NPs/Al was studied where an efficiency of 3.97 % is achieved through standard procedures. Interestingly, byomitting the ETL in the simulations leads to a substantial efficiency of 10.83 % after optimization. This increased efficiency demonstrates an economically feasible solar cell structure. Improved photovoltaic performance may arise from additional research and optimisation of BHJPSC designs without ETL.

 $\textit{Keywords:}\ \text{bulk heterojunction polymer solar cell, SCAPS 1-D, HTL, Fullerene bisadduct IC}_{60}\,\text{BA}.$

Classification numbers: 3.4.1, 4.10.4

1. INTRODUCTION

Non-conventional energy sources are essential when energy demands rise and conventional fossil fuels become less common. Bulk heterojunction polymer solar cells (BHJ PSCs) have

recently received increased attention as a possible renewable energy source due to their simple fabrication technique, low cost, light weight nature, and adaptability [1 - 3]. The active layer of these solar cell devices typically consists of two organic semiconductor materials: an electron acceptor (n-type fullerene derivatives) and an electron donor (p-type conjugated polymer) [4]. The unique features of "small molecule organic or polymer solar cells", QD sensitised solar cells (QD-SSCs) (Ghoreishi *et al.*, 2014) have further led to their appeal [5 - 9].

Poly(3-hexylthiophene) (P3HT) is an important material for electron donation in bulk heterojunction (BHJ) polymer solar cells because of its good hole mobility, stable with the environment and absorption in the extended red light. One of the most popular electron acceptors is [6,6]-phenyl-C61-butyric acid methyl ester (PCBM) [10-12], which has low LUMO energy levels and provides an open circuit voltage of just over 0.6 V [13] . Of late, there has been a push to use the indene-C60 bis adduct (IC $_{60}$ BA), which has higher LUMO energy levels and provides for the open circuit voltage of about 0.84 V, along with more efficiency [14 - 18].

Bulk heterojunction polymer solar cells (BHJPSCs) are beneficial to photovoltaic technology because they are inexpensive and quick to manufacture. The bulk heterojunction (BHJ) structure allows for rapid exciton dissociation by utilizing a bicontinuous network of donor and acceptor materials. Bendenia et al. demonstrated that an all polymer blend resulted in excellent photogeneration [19]. The BHJ structure was first described by Heeger and co-workers in 1995 for polymer fullerenes blends [20], and this is where we find that additives can ultimately increase the domain sizes of the donor and acceptor materials and improve performance [21, 22]

To enhance the performance of bulk heterojunction (BHJ) polymer solar cells (PSCs), Li et al. studied indene-C60 bis adduct ($IC_{60}BA$) as an electron acceptor to address the issue of low open circuit voltage (Voc) of the P3HT:PCBM blend [23]. In an experiment with P3HT:IC₆₀BA, they achieved high power conversion efficiencies (PCE) and a Voc value of 0.84 V [24 - 25]. The authors modelled the solar cells using SCAPS 1-D software and validated the model against experiment [26 - 27]. In this case, the hole transport layer was PEDOT:PSS and the active layer was P3HT:IC₆₀BA.

In polymer solar cells, electron transport layers (ETL) are used for collecting the electrons but could limit the performance of the device because of issues with the material such as TiO_2 degrading from UV light or trapping the electrons because of defects in the layer. Studies have shown that removing the ETL can create an increase in efficiency and lower the cost of production. In some cases, the performance of the ETL materials can be greatly affected by lowering the thickness of the layer, so the material becomes a scalability issue for mass production. An optimization of a standard structure replaced without ETL [ZnO nanoparticles] leads to a most significant enhancement of the efficiency from structures with ETL proving evidence to high efficiency polymer solar cells.

2. DEVICE SIMULATION METHODOLOGY

This study used the one-dimensional Solar Cell Capacitance Simulator-SCAPS version (3.3.08). Engineers and researchers benefited from its unique features and enhancements. SCAPS-1D 3.3.08 characteristics are listed below. It solves the optical and electrical models for the full arrangement. SCAPS-1D users can describe their solar cell structure by specifying layers. Each layer can have varied dielectric constant, electron affinity, thickness, and bandgap. Users can enter own material specifications; however, the software has a library of solar cell materials. SCAPS-1D calculates carrier transport via drift-diffusion. This model accounts for

electric field drift and carrier concentration gradient diffusion. The SCAPS-1D device simulation tools enable to model recombination mechanisms by fully specifying defect states. The bulk defect states can be specified with an energy distribution, density of states, and electron and hole capture cross-sections within the bulk of each semiconductor layer. The interface defect states can also be specified at the heterojunctions, with properties unique to each of those interface defect states. The bulk defect states and interface defect states can be parameterized to obtain Shockley-Read-Hall (SRH) recombination rates, which will yield a better representation of your device's electrical behaviour. The software simulates solar cell layer light absorption and electron-hole pair production. SCAPS-1D can simulate varied light intensities and spectrum distributions (AM1.5G, monochromatic, etc.).

The software simulates the I-V characteristics of solar cells under varying conditions. generating outputs such as Voc [Open circuit voltage], Jsc [Short circuit current], FF[Fill factor], and PCE[Power conversion efficiency]. Multi-junction solar cells, which can absorb more sunlight by having a stack of multiple layers with bandgaps, can also be simulated. An intuitive GUI helps shorten the time to setup simulations, adjust parameters, and view results using SCAPS-1D. Result files can be saved in many different types of formats for later analyses, and graphs can be edited and saved for the reporting component. SCAPS-1D allows users to perform sensitivity analysis to see how variations in parameters can affect solar cell performance. For organic solar cells software is used for exploring various donor-acceptor material combinations and their impact on device efficiency and it was found that the ratio of donor to acceptor materials critically affects charge transport and recombination rates. Optimal blend ratios were determined for enhanced efficiency. In our study, we have used a 1.5 AM spectrum for illumination. Previous simulations have been performed on fullerene and non-fullerene BHJ, perovskite, and tandem solar cells (Abdelaziz et al., 2019, 2020; Gupta and Dixit, 2018; Bahrami et al., 2019). In their study in 2019, Abdelaziz et al. focused on the simulation and optimization of lead-free perovskite solar cells using SCAPS-1D software. They investigated the performance of a solar cell structure composed of FTO/TiO₂/CH3NH3SnI3/Spiro-OMeTAD/Au. Their primary objective was to enhance the cell efficiency by optimizing the thickness of the absorber layer and the defect density. The simulation results highlighted that optimizing these parameters significantly improved the power conversion efficiency (PCE) of the solar cells.

SCAPS-1D possesses multiple control panels for parameter variation and thin film solar cell simulation. Each of the control panels serves to simplify the management and tuning of a simulation by targeting a single simulation step. Project files (multiple simulations) can be created, saved, and retrieved in the main control panel. The simulation run control panel is where the initiation of simulation, pause, and simulation control takes place. The device construction panel is where layers of the solar cell can be added, deleted, and defined. Depending on the material property panel the user can select the bandgap, electron affinity, and dielectric constants for each material layer. The user has the ability to select carrier mobility, recombination and diffusion coefficients. In the defects and recombination panel, energy levels (and densities), and capture cross-sections for the electron and hole can be selected to specify bulk defect state in the material. The user can select to define the SRH, radiative, and Auger recombination parameters. In the lighting and optical properties panel users can select the type and intensity of lighting source and confirm their designs against AM1.5G physical sun spectra or to define a light source spectral distribution specifically. Each layer's reflectance and absorption coefficients affect light absorption and the device's functionality. The electrical simulation allows the user to select forward and reverse biases. The temperature settings panel allow the temperature settings to be defined for the simulated operating temperatures.

The output and results panel display graphical outputs such as I-V curves, C-V curves, and OE spectra. Users can customize the graphs, zoom in on specific regions, and compare multiple simulations. The data export tool helps in exporting simulation results to various formats (e.g., CSV) for further analysis. These control panels are designed to provide a comprehensive and user-friendly interface for setting up and managing solar cell simulations. By organizing the software into these specific panels, the SCAPS-1D ensures that users can easily find and adjust the parameters they need for their specific simulation requirements.

SCAPS-1D numerically solves the coupled Poisson and continuity equations iteratively to yield a steady-state operating point in equilibrium for the general semiconductor equations. Before and after deployment of the stimulus, the general semiconductor equations, [e.g. Poisson's equations, continuity equations, drift and diffusion current equations], are very quick in determining the electrical performance of the electronic device. Ultimately the electrical performance is derived from potential, photons, or thermal energy as sourced from the stimulus. The device electrical performance and I-V characteristics are formulated through these equations. Therefore, this provides the theoretical method for investigation and understanding device performance. The Poisson equations express the electrostatic potential with semiconductor charge distributions [Equation 1]. The continuity equations express charge conservation with holes and electrons [Equations 2-3]. The drift-diffusion equations express the electron and hole current densities [Equations 4-5]. The finite difference method (FDM) discretizes the semiconductor equations on a one-dimensional grid. The equations are solved at discrete grid nodes across the one-dimensional grid sections of the device. Initial guesses of the electrostatic potential and carrier concentrations are obtained. The guess may come from equilibrium conditions or previous simulations will provide a more informed guess. For boundaries at the contacts, Dirichlet or Neumann boundary conditions are applied (prescribed potential or prescribed current density). At the interfaces of materials, the potentials and current densities are continuous. The numerical iterative methods such as the Newton-Raphson Method and Gummel Iteration solve the coupled systems of nonlinear algebraic equations from discretization. The Newton-Raphson Method linearizes the nonlinear equations about the guess and solves the linear system iteratively. The Poisson's equation for potential and the continuity equations for carriers are solved alternatively. The total device current is computed from the numerically integrated current densities across the cross sectional area of the device. The total device current is derived at a corresponding potential. The I-V curve is computed by varying actual potential application and repeating the solution. They will also analyze and predict the performance of new architectures, save significant human resources, time, and money on experiment costs.

$$\frac{\partial \varepsilon_0 \varepsilon}{\partial x} \frac{\partial \Psi}{\partial x} = -q \left(p - n + N_D - N_A + \frac{\rho_{def}}{q} \right) \tag{1}$$

$$-\frac{\partial J_n}{\partial x} - \text{Un} + G = \frac{\partial n}{\partial t}$$
 (2)

$$\frac{\partial J_n}{\partial x} - \text{Un} + G = \frac{\partial n}{\partial t}$$

$$\frac{\partial J_p}{\partial x} - \text{Up} + G = \frac{\partial p}{\partial t}$$

$$J_n = -\frac{\mu_n n}{q} \frac{\partial E_{Fn}}{\partial x}$$

$$J_p = +\frac{\mu_p p}{q} \frac{\partial E_{Fp}}{\partial x}$$
(5)

Equations, the charge is denoted by a The fundamental charge

$$Jn = -\frac{\mu_n n}{q} \frac{\partial E_{Fn}}{\partial x} \tag{4}$$

$$Jp = +\frac{\mu_p p}{q} \frac{\partial E_{Fp}}{\partial x} \tag{5}$$

In the above-mentioned equations, the charge is denoted by q. The fundamental charge of an electron is approximately 1.602×10⁻¹⁹ C. It is a constant used in all the equations involving charge carriers (electrons and holes). Ψ denotes the electrostatic potential which represents the electric potential energy per unit charge at a point in the semiconductor. It is a solution to the Poisson equation and influences the movement of charge carriers. The symbols p, n, pt, and nt stand for free holes and electrons concentrations (number of electrons or holes per unit volume), trapped holes and trapped electrons which represent holes and electrons captured by traps, respectively. N_D (donors that have released an electron and become positively charged) and N_A (acceptors that have captured an electron and become negatively charged) denote ionized donor-like and ionized acceptor-like doping concentrations, respectively. Here, ϵ signifies absolute permittivity, while ϵ_0 denotes permittivity in free space which represents the ability of the material to permit electric field lines. It influences the electric potential distribution within the material. In and Jp signify electron and hole current densities which are derived from the drift and diffusion components of carrier transport, respective while Un denotes electron recombination rate, Up is the rate of hole recombination (The rate at which electrons and holes recombine and annihilate each other), and G is the generation rate (The rate at which electronhole pairs are generated, typically by absorption of photons in the context of solar cells). In contrast to what has been described so far, E_{Fn} and E_{Fp} stand for the electron and hole quasi-Fermi levels, whereas μ_n and μ_p indicate the electron and hole mobility, respectively. In SCAPS-1D software, understanding the concepts of assumed Fermi energy levels (E_{Fn}, E_{Fp}) and the conductivity of electrons and holes (n, p) is crucial for analyzing the behavior of semiconductor devices. In thermodynamic equilibrium, the Fermi level is the energy level at which the probability of finding an electron is 50 %. It represents the chemical potential for electrons in the system. In non-equilibrium conditions (e.g., when a device is illuminated or under bias), separate quasi-Fermi levels are defined for electrons (E_{Fn}) and holes (E_{Fn}) . When there are nonequilibrium conditions, the energy level E_{Fn} corresponds to the distribution of electrons in the conduction band, and the corresponding energy level E_{Fp} corresponds to the distribution of holes in the valence band. These quasi-Fermi levels are crucial for determining the carrier concentrations (n and p) and the current flow in the device. In equilibrium, E_{Fn} and E_{Fp} coincide with the overall Fermi level (E_F), as there is no net generation or recombination. Under illumination or bias, E_{Fn} and E_{Fp} split, reflecting the different energy distributions of electrons and holes. The splitting is a measure of the deviation from equilibrium and is related to the applied voltage and light-generated carriers. The conductivity attributed to holes is increased by higher hole concentration (p) and mobility (μ_p) , whereas the conductivity attributed to electrons is increased by higher electron concentration (n) and mobility (μ_n).

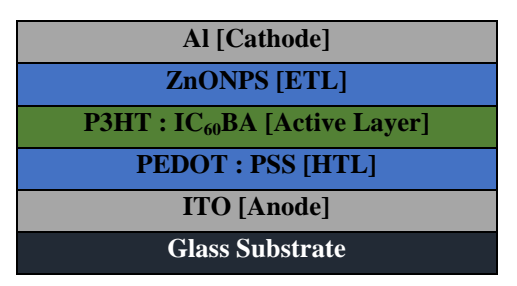


Figure 1. Simulated bulk heterojunction polymer solar cell structure.

Figure 1 depicts the configuration of the simulated bulk heterojunction structure, which is Glass substrate/ITO/PEDOT: PSS/P3HT:IC $_{60}$ BA/ZnONPS/Al. Table 1 shows the material parameters used in the simulation, including electron affinity (χ), bandgap energy (Eg), and relative permittivity (ϵ r). The mobilities for holes and electrons are μ_p and μ_n , respectively. N_D and N_A represent donor and acceptor density, respectively. Nv and Nc represent the effective

density of states in the valence and conduction bands, respectively, whereas Nt represents the defect density. The anode and cathode work functions are set at 4.8 and 4.2 eV, respectively. The thermal velocity is set to 10^7 cm/s, and the capture cross section for holes and electrons is set to 1×10^{-25} cm² across all layers. As already mentioned, the main output parameters of solar cell are Voc , Jsc , FF and PCE . The required material parameters for simulation and absorption spectra are gathered from the literature [26 - 28, 29 - 37]. Table 2 shows the comparative evaluation of experimental and simulated values for calibrating SCAPS 1-D

Parameter	HTL	Active layer	ETL
Thickness [nm]	27	250	46
Eg (eV)	1.6	1.68	3.2
χ (eV)	3.4	3.880	4.6
εr	3.0	3.3	9.0
$\mu_{\rm n}~({\rm cm^2/vs})$	10 ¹	10 ⁷	10 ⁷
μp (cm ² /vs)	400	10 ⁷	10 ⁷
$N_A (cm^{-3})$	10 ¹⁵	0	0
$N_D (cm^{-3})$	0	3.2×10^{18}	1.1×10^{18}
$N_{\rm C}$ (cm ⁻³)	2.2×10^{15}	1.6×10^{20}	2.2×10^{19}
$N_V (cm^{-3})$	1.8×10^{18}	10 ¹⁹	1.8×10^{19}
N _t (cm ⁻³)	10^{15}	10^{16}	10 ¹⁵

Table1. Simulation parameters of bulk heterojunction polymer solar cell.

Table 2. Evaluation of simulated parameters with experimentalresults.

Parameter	Experimental	Simulated
Voc (V)	0.84	0.85
Jsc (mA/cm ²)	8.36	8.21
FF (%)	59	57
PCE (%)	4.1	3.97

3. RESULTS AND DISCUSSION

3.1. Effect of active layer thickness

The active layer thickness is varied between 300 nm to 700 nm. As thickness increases, Voc, Jsc and PCE increase, but FF decreases. The corresponding graph is given in Figure 2. Voc increases due to the production of more charge carriers. Variation in Jsc accounts for more light absorption and FF declines due to increase in series resistance and recombination. Variation in PCE accounts for the combined effect of all other output parameters

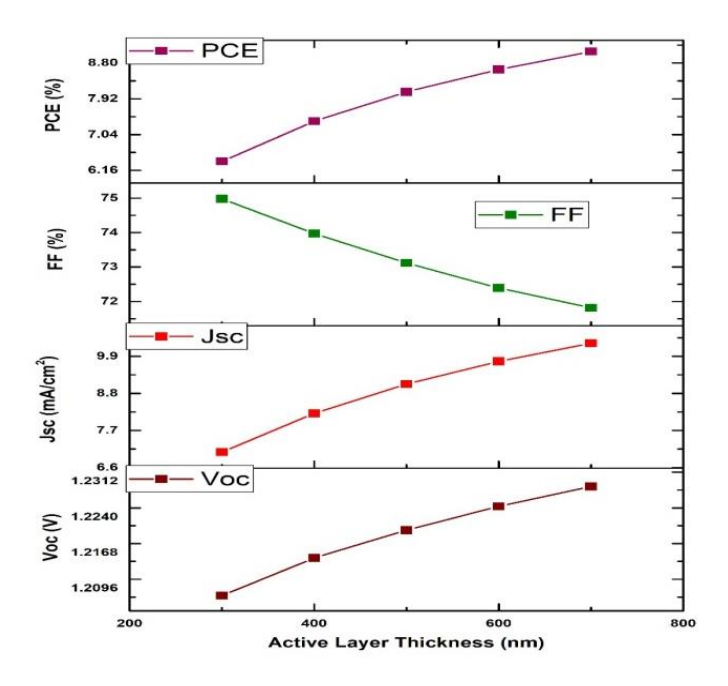


Figure 2. Influence of active layer thickness on cell performance.

3.2. Effect of shallow defect density of active layer

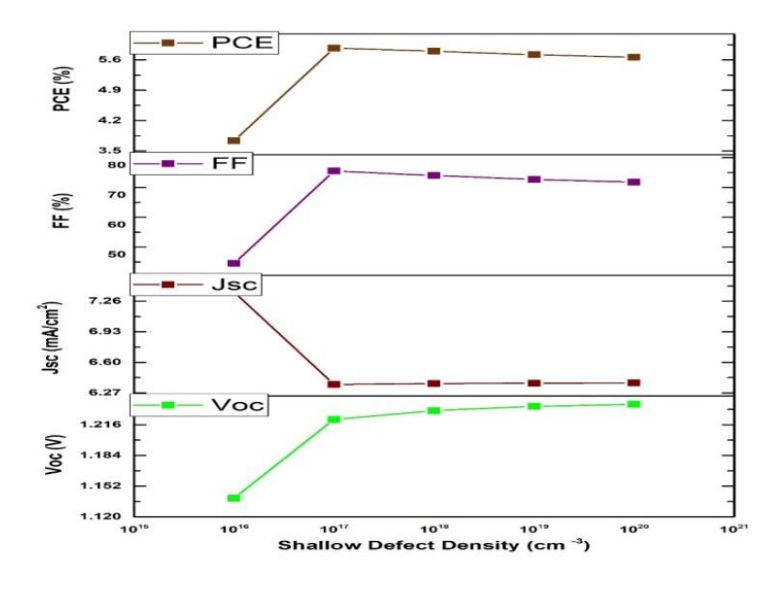


Figure 3. Influence of shallow defect density on cell performance.

The shallow defect density of the active layer is increased from $10^{16}~\rm cm^{-3}$ to $10^{20}~\rm cm^{-3}$. Voc is found to increase with shallow defect density, although FF and PCE vary similarly. Jsc is found to decrease with increasing shallow defect density. Optical techniques based on subbandgap absorption or emission can also provide insights into the defect density in the active layer. It was discovered that optimal performance occurs at $10^{17}~\rm cm^{-3}$, with an efficiency of

5.87 %. These variances are depicted in Figure 3. Shallow defect density can act as trapping sites, leading to non-radiative recombination which impacts the Voc. The Jsc is lowered by high defect density due to increased recombination and trapping of charge carriers. FF is decreased due to increased recombination and localized resistive losses, at high defect density. Reductions in Voc, Jsc, and FF results in the variation of PCE. Improved material purity, optimized fabrication processes, and careful control of the polymer morphology helps in reducing shallow defect density for better performance

3.3. Effect of temperature

The temperature is changed from 300 K to 360 K. The optimal performance is achieved at 300 K. The variations of output parameters are depicted in Figure 4.

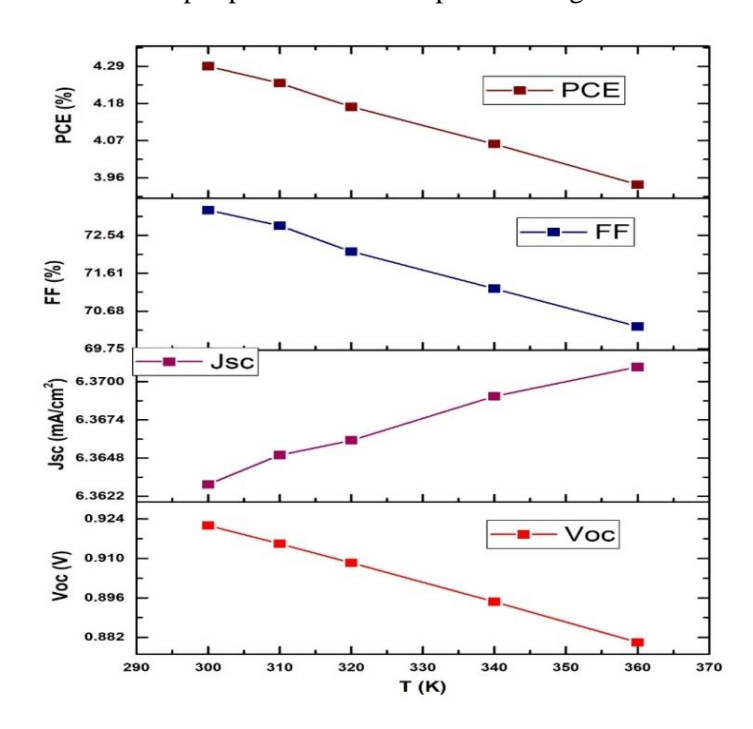


Figure 4. Influence of temperature on cell performance.

At higher temperatures, the materials carrier concentrations, mobility of charge carriers, resistance, and bandgap changes. As temperature rises, the intrinsic carrier concentration in the semiconductor increases, leading to a reduction in the separation of the quasi-Fermi levels. This results in a decrease in Voc. Additionally, increased temperature can enhance the recombination rates of charge carriers, further lowering Voc. Jsc increases with increasing temperature due to enhancement in the mobility of charge carriers and slightly increase in absorption of photons. Elevated temperatures increase the series resistance and decrease the shunt resistance in the solar cell leading to the reduction in FF. The diode ideality factor also increases with temperature, negatively impacting the FF. Since PCE is a product of Voc, Jsc, and FF, the overall efficiency tends to decrease with rising temperature. Maintaining the efficiency of polymer solar cells requires proper thermal management, which includes choosing materials with improved thermal stability to lessen the negative impacts of temperature rise, using heat sinks, and optimising cell

design. In polymers, thermally generated carriers increase with temperature, enhancing the overall carrier concentration.

3.4. Effect of electron affinity of active layer

The electron affinity of the active layer ranges from 3.5eV to 4 eV. Simulation revealed an optimal value of 5.75 % efficiency for 3.7 eV electron affinity. This is due to the enhancement in exciton dissociation, charge transport and reduction in recombination losses. Figure 5 shows a graphical illustration. If the electron affinity of the acceptor is high, it ensures a larger energy difference, potentially increasing Voc. However, if the electron affinity is too high, it may also increase recombination rates, which could negate the benefits. A higher electron affinity can facilitate better electron transport to the electrode, reducing recombination within the active layer. This enhances the overall charge collection efficiency, contributing to higher Jsc and FF. Conversely, if the electron affinity is not optimized, it can lead to poor charge transport and higher recombination losses. Proper electron affinity ensures optimal energy level alignment, facilitating efficient charge transfer. Optimized electron affinity enhances charge transport and reduces recombination, improving Jsc and FF. Wellmatched electron affinity reduces recombination losses, enhancing overall device efficiency.

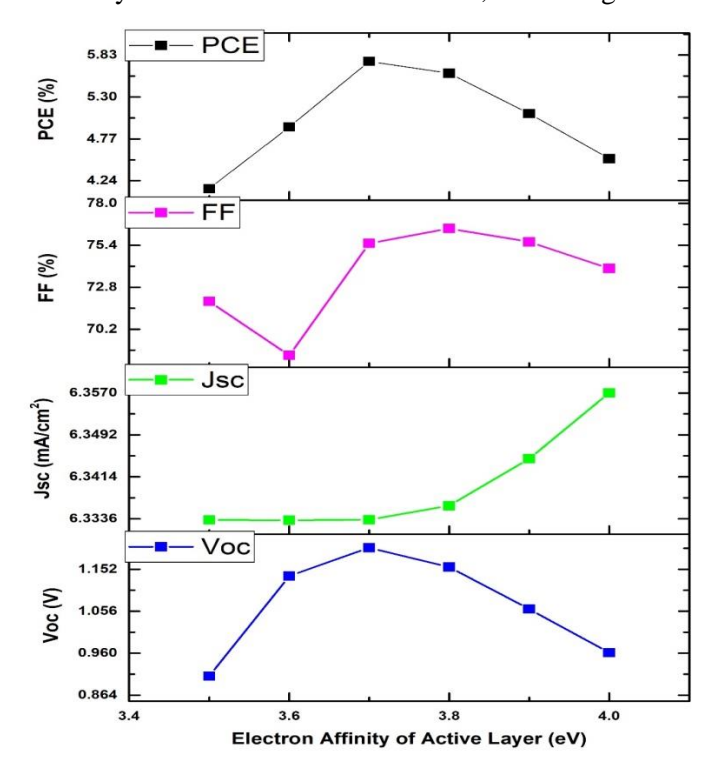


Figure 5. Influence of electron affinity of active layer on cell performance.

3.5. Effect of carrier concentration of active layer

The carrier concentration of the active layer is increased from 10¹⁷ cm⁻³ to 10²¹ cm⁻³. In this study, we discovered that Voc reaches its maximum value of 1.2013 V, whereas PCE reaches its maximum value of 5.76 % at 10¹⁸ cm⁻³. Jsc achieves its maximum value of 6.333860 mA/cm²,

whereas FF achieves its greatest value of 76.08 % at 10^{21} cm⁻³. Figure 6 shows the corresponding graph. Increased doping concentration can lead to better alignment of energy levels, reducing recombination losses and potentially increasing Voc. Proper doping can enhance the electrical conductivity and mobility of charge carriers, improving their transport to the electrodes and increasing Jsc

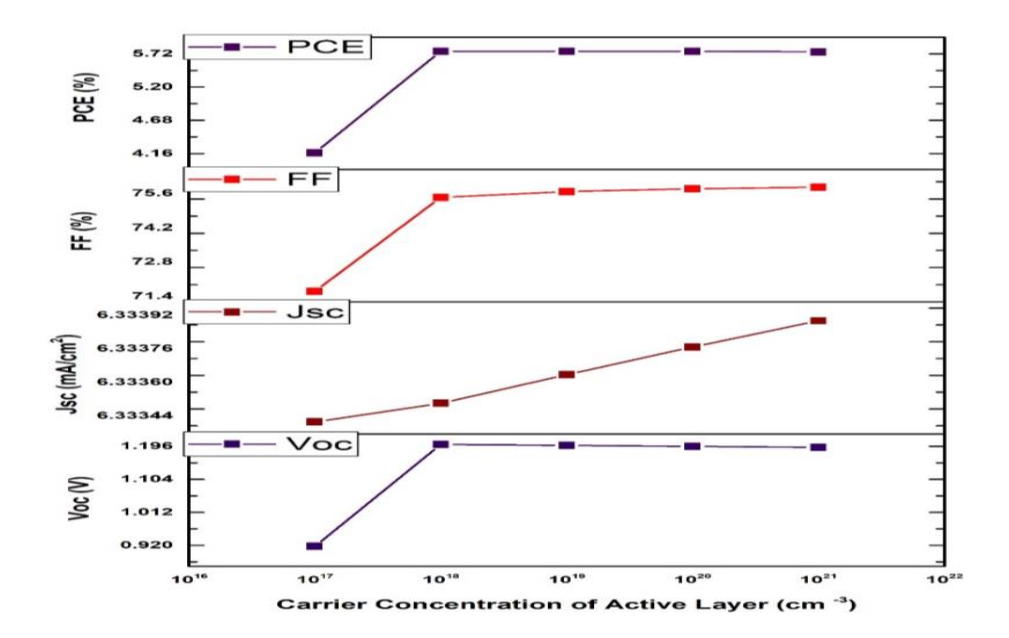


Figure 6. Effect of carrier concentration of active layer on cell performance.

Appropriate doping levels can decrease the series resistance (by increasing conductivity) and minimize shunt pathways (by reducing defects), thereby increasing the FF. Optimal doping improves Voc, Jsc, and FF, leading to higher PCE. To maximize the performance of polymer solar cells, it's crucial to optimize the doping concentration. This involves finding a balance where the doping is sufficient to improve electrical properties and charge transport but not so high as to introduce significant recombination losses or defects.

3.6. Influence of thickness of hole transport layer

The thickness of hole transport layer [HTL] is changed from 25 nm to 45 nm. The optimized values are obtained for a thickness of 30 nm. The corresponding diagram is given in Figure 7. An optimal HTL thickness ensures efficient hole transport and extraction, maintaining a high built-in potential and resulting in a higher Voc. An appropriately thick HTL allows for efficient hole transport to the anode without significant recombination losses, leading to a higher Jsc. A very thick HTL increases series resistance, reducing the FF. An optimal HTL thickness improves Voc, Jsc, and FF, leading to a higher PCE.

3.7. Effect of band gap of HTL

The band gap of HTL varies from 1.4 eV to 1.8 eV. It was discovered that Voc, FF, and PCE rise with the band gap and achieve optimal performance at 1.8 eV. Figure 8 depicts the variations in the output parameters. Voc is a direct consequence of bandgap, with a higher

bandgap resulting in higher Voc and a lower rate of radiative recombination. Jsc drops with increasing bandgap due to reduced production of electrons, as few photons have enough energy. An HTL with an appropriate band gap ensures proper energy level alignment with the active layer, minimizing energy losses during hole extraction resulting in a higher Voc. A mismatched band gap can create energy barriers, hindering hole extraction and leading to increased recombination, which reduces Jsc. A properly aligned band gap minimizes recombination and series resistance, leading to a higher FF. An optimal HTL band gap ensures efficient charge extraction and minimal recombination, maximizing Voc, Jsc, and FF, and thus PCE. To maximize the performance of polymer solar cells, the HTL band gap should be optimized to align well with the energy levels of the active layer.

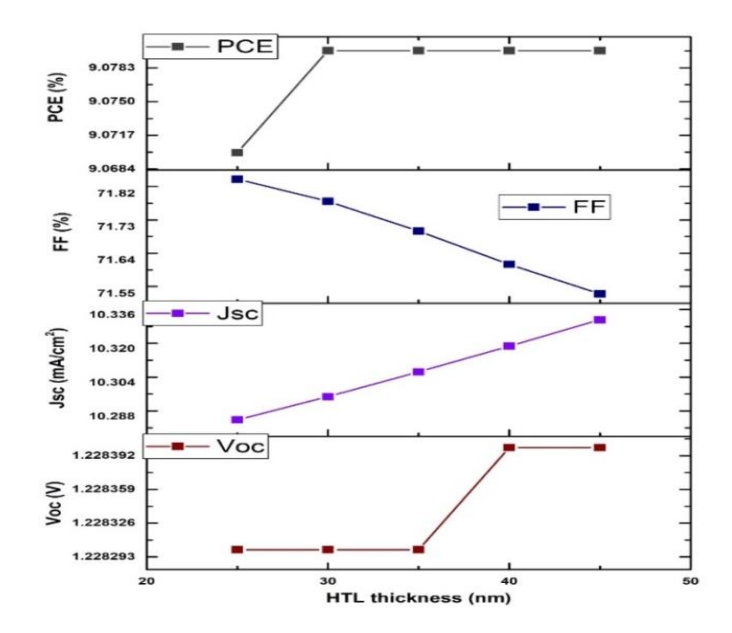


Figure 7. Influence of thickness of HTL.

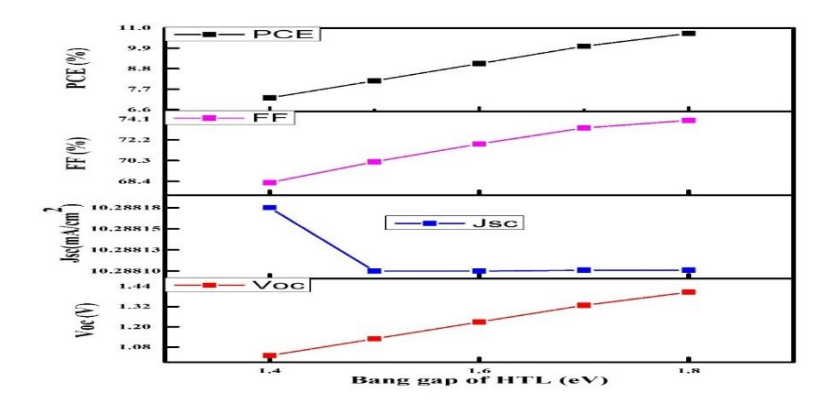


Figure 8. Influence of Band Gap of HTL on cell performance.

3.8. Influence of electron affinity of HTL

The electron affinity of HTL ranges from 3.2 eV to 3.6 eV. The optimal performance is achieved at 3.4 eV. Figure 9 shows the respective changes in the output parameters. An HTL with suitable electron affinity will align its energy levels with the active layer, preventing electron leakage and recombination at the HTL/anode interface. If the electron affinity is mismatched, it can cause inefficient charge separation and increased recombination losses, reducing Jsc. Proper electron affinity reduces recombination losses and ensures efficient charge transport, leading to a higher FF at 3.4 eV. A high electron affinity can increase recombination rates and resistive losses, reducing the FF. An optimal electron affinity ensures efficient charge separation and transport, maximizing Voc and FF, leading to a higher PCE at 3.4 eV. Mismatched electron affinity can result in suboptimal Voc, Jsc, and FF, thereby reducing the overall PCE. To maximize the performance of polymer solar cells, the electron affinity of the HTL should be optimized to ensure proper energy level alignment with the active layer and the anode

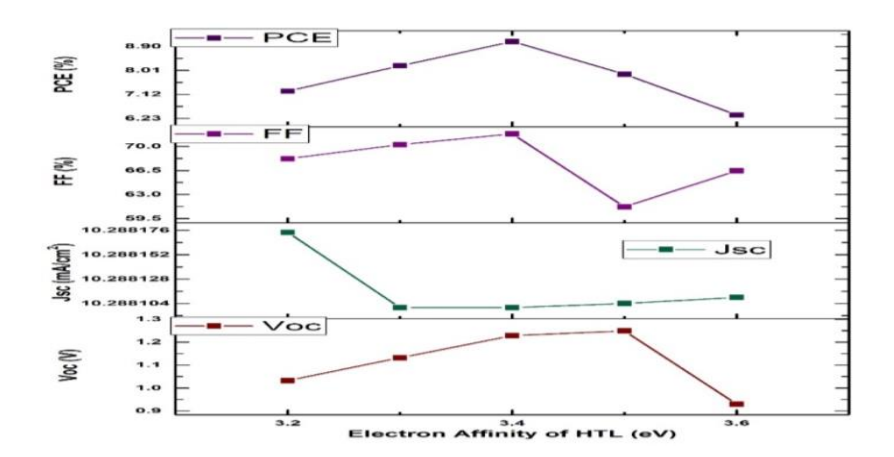


Figure 9. Effect of electron affinity of HTL on cell performance.

3.9. Effect of effective density of states [CB] of HTL

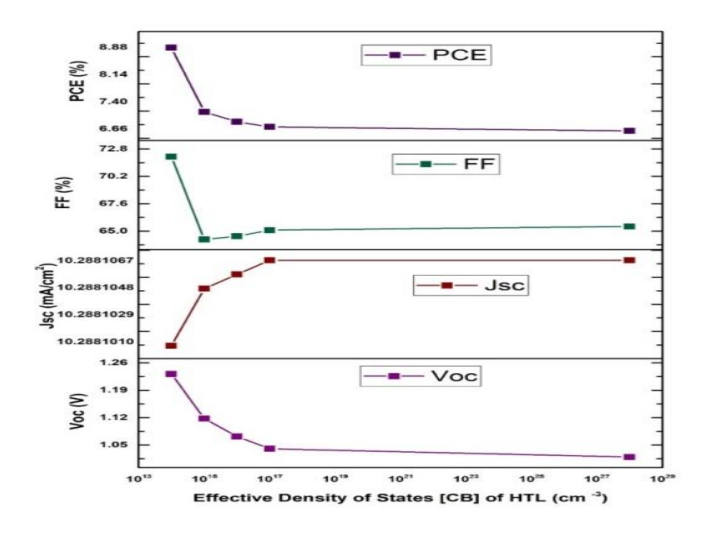


Figure 10. Influence of density of states [CB] of HTL.

The effective density of states of conduction band of HTL is changed from 10^{14} cm⁻³ to 10^{18} cm⁻³. In this case, Voc and PCE decrease as the density of states increases. Jsc is found to increase while FF initially decreases, then increases. The optimized performance is obtained at 10^{14} cm⁻³. The corresponding graph is given in Figure 10.

3.10. Influence of effective density of states [VB] of HTL

The effective density of states of valence band of HTL is changed from 10^{16} cm⁻³ to 10^{20} cm⁻³. Here, the Voc, FF and PCE decrease as the effective density of states in the valence band of HTL increases. Jsc is found to increase with the effective density of states in the valence band of HTL. The optimized results are obtained at 10^{16} cm⁻³. The results are shown in Figure 11.

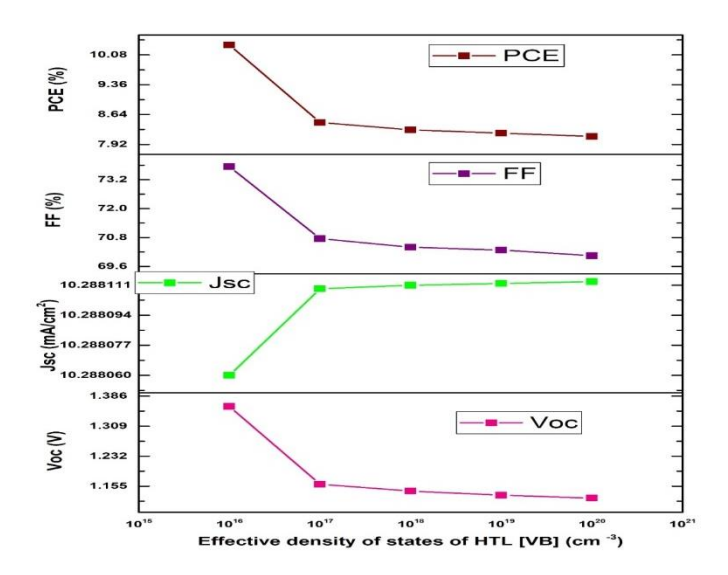


Figure 11. Influence of density of states [VB] of HTL.

3.11. Effect of shallow acceptor density of HTL

There is an increase in the shallow acceptor density of states of HTL from 10^{14} cm⁻³ to 10^{18} cm⁻³. In this case, it is discovered that Voc increases as HTL acceptor density increases, whereas FF and PCE drop as HTL shallow acceptor density increases. An acceptor density of 10^{14} cm⁻³ yields the best results. The graphs are displayed in Figure 12. The Voc is enhanced by improving the built-in potential and reducing recombination losses. The Jsc is increased with efficient hole transport and minimal recombination. The FF is reduced due to increase in series resistance and recombination. The PCE is maximized when Voc, Isc, and FF are optimized through balanced HTL doping density. To maximize the performance of polymer solar cells, the doping density in the HTL should be optimized. This involves finding a balance where the HTL is doped enough to improve hole mobility and transport while minimizing recombination and resistive losses. Achieving this balance ensures that the solar cell operates efficiently with high Voc, Jsc, FF, and PCE.

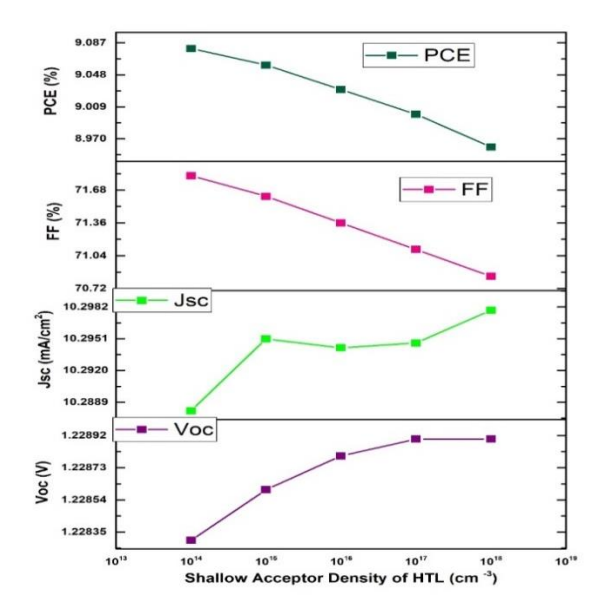


Figure 12. Effect of shallow acceptor density of HTL.

3.12. Influence of defect density of HTL

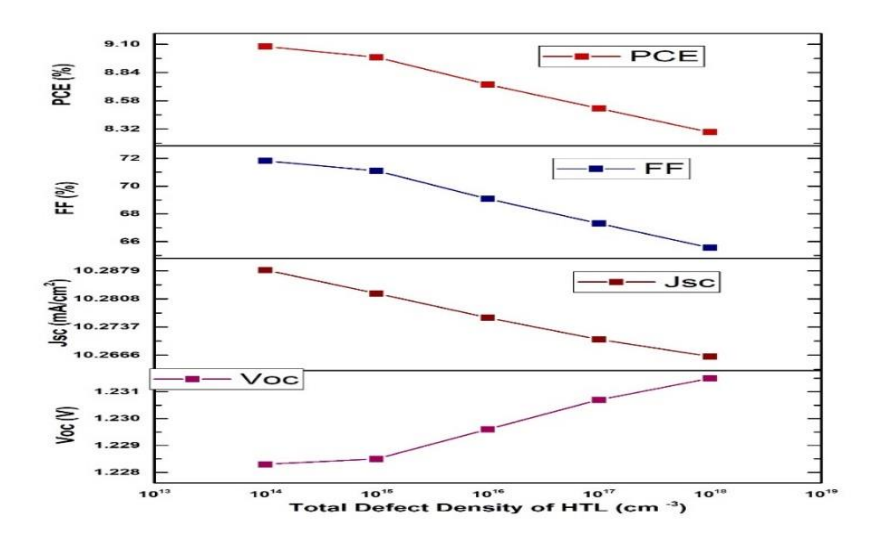


Figure 13. Effect of total defect density of HTL on cell performance.

The total defect density of HTL is changed from 10¹⁴ cm⁻³ to 10¹⁸ cm⁻³. Here, the Voc is found to increase, while the other output parameters are found to decrease as the total defect density of HTL increases. The optimized performance is obtained at a defect density of 10¹⁴ cm⁻³. The corresponding graph is given in Figure 13. In polymer solar cells, defects in the HTL can act as recombination centers where charge carriers (electrons and holes) can recombine. When the defect density increases, it can lead to more effective trapping of electrons that have diffused into the HTL. This trapping can reduce the rate of recombination of photogenerated charge carriers at the HTL interface, leading to a lower overall recombination rate in the cell. Reduced recombination of charge carriers helps maintain a higher separation of charges, thereby

increasing the quasi-Fermi level splitting and resulting in a higher Voc. A high defect density can trap charge carriers, reducing their mobility and increasing recombination rates, which lowers the Jsc. High defect density increases the series resistance due to impeded charge transport and introduces more shunt pathways through increased recombination, both of which reduce the FF. Lower defect density ensures efficient charge transport and collection, minimal recombination losses, and optimal series and shunt resistances, thereby maximizing Voc, Isc, and FF, and consequently the PCE. Higher defect density has the opposite effect, reducing all these parameters and thereby lowering the PCE. Careful material selection, processing conditions, and interface engineering are adopted to reduce the defect density

4. CONCLUSIONS

Numerical investigations were conducted on a fullerene BHJ PSC employing the ITO/PEDOT:PSS/P3HT:IC $_{60}$ BA/ZnONPs/Al structure. These studies were validated by comparing the simulated results with experimental data from the literature. Remarkably, the actual device performance closely mirrored the simulated outcomes. Our study examines the impact of parameters such as hole transport layer characteristics, absorber layer thickness, doping concentration, defect density, and temperature on cell performance, specifically focusing on configurations devoid of an electron transport layer (ZnO NPs). Through optimization, we enhanced parameters to augment the power conversion efficiency (PCE). Notably, the optimization process included fine-tuning transport layer properties. The resultant cell performance with optimized numerical parameters yielded: Voc = 1.4158 V, Jsc = 10.294741 mA/ cm², FF = 74.30 %, and PCE = 10.83 %. The results are encouraging and may open up future research in this field.

Acknowledgements. The authors would like to acknowledge Pr.M. Burgelman, University of Gent, Belgium for providing the SCAPS 1-D software for the simulation study.

CRediT authorship contribution statement. All authors contributed equally to this work.

Declaration of competing interest. The authors declare that they have no known competing financial interests or personal relationships that could have appeared to influence the work reported in this paper.

REFERENCES

- 1. Mohd Yusoff A. R., Silva W. J., Schneider F. K. Understanding the ph-dependent ehaviour of graphene oxide aqueous solutions on organic photovoltaic performance, Solar Energy Materials and Solar Cells **194** (2019) 62-66.
- 2. Cui C., Wong W. Y., Li Y. Improvement of open-circuit voltage and photovoltaic properties of 2d-conjugated polymers by alkylthio substitution, Energy & Environmental Science **7** (7) (2014) 2276-2284.
- 3. Singh T. J., Singh S., Islam S. M., Mahala P., Singh K. J. Flexible organic solar cells with graphene/pedot: Pss schottky junction on pet substrates, Optik **181** (2019) 984-992.
- 4. Urbina A., Abad J., Romero A. J. F., Lacasa J. S., Colchero J., Gonz'alez-Mart'inez J. F., Rubio-Zuazo J., Castro G. R., Gutfreund P. Neutron reflectometry and hard x-ray photoelectron spectroscopy study of the vertical segregation of pcbm in organic solar cells, Solar Energy Materials and Solar Cells **191** (2019) 62-70.

- 5. Riede M., Spoltore D., Leo K. Organic solar cells-the path to commercial success, Advanced Energy Materials **11** (1) (2021) 2002653.
- 6. Deibel C., Dyakonov V. Polymer–fullerene bulk heterojunction solar cells, Reports on Progress in Physics **73** (9) (2010) 096401.
- 7. Xu M., Wei C., Zhang Y., Li H., Ma J., Lin J., Wang S., Xue W., Wei Q., Xie L., *et al.* Ultrafast photoexcitation dynamics behavior of hydrogen-bonded polyfluorenol, Chinese Chemical Letters **35** (1) (2024) 108279.
- 8. Ghoreishi F., Ahmadi V., Samadpour M. Journal of Power Sources 271 (2014) 195.
- 9. Ghadiri E., Taghavinia N., Zakeeruddin S. M., Gratzel M., Moser J. E. Enhanced electron collection efficiency in dye-sensitized solar cells based on nanostructured TiO₂ hollow fibers, Nano letters **10** (5) (2010) 1632-1638.
- 10. He Y., Zhao G., Peng B., Li Y. High-yield synthesis and electrochemical and photovoltaic properties of indene-c70 bisadduct, Advanced Functional Materials **20** (19) (2010) 3383-3389.
- 11. Bendenia C., Merad-Dib H., Bendenia S., Hadri B. Numerical modelisation of zno interfacial layer on p3ht: Pcbm based organic photovoltaic bulk heterojunction devices, Optik **174** (2018) 167-172.
- 12. Hazra A., Mal I., Samajdar D., Das T. Analytical modelling of organic solar cells with scattering interface, Optik **168** (2018) 747-753.
- 13. Sun Y., Cui C., Wang H., Li, Y. Efficiency enhancement of polymer solar cells based on poly (3-hexylthiophene)/indene-c70 bisadduct via methylthiopheneadditive, Advanced Energy Materials 1 (6) (2011) 1058-1061.
- 14. He Y., Chen H. Y., Hou J., Li Y. Indene- c60 bisadduct: a new acceptor for high-performance polymer solar cells. Journal of the American Chemical Society **132** (4) (2010) 1377-1382.
- 15. Zhao G., He Y., Li Y. 6.5 % efficiency of polymer solar cells based on poly (3-hexylthiophene) and indene-c60 bisadduct by device optimization, Advanced Materials **22** (39) (2010) 4355-4358
- 16. Tan Z., Qian D., Zhang W., Li L., Ding Y., Xu Q., Wang F., Li Y. Efficient and stable polymer solar cells with solution-processed molybdenum Oxideinterfacial layer, Journal of Materials Chemistry A 1 (3) (2013) 657-664.
- 17. G"artner S., Christmann M., Sankaran S., R"ohm H., Prinz E. M., Penth F., P"utz A., T"ureli A. E., Penth B., Baumst"ummler B., *et al.* Eco-friendly Fabrication of 4 % efficient organic solar cells from surfactant-free p3ht: Icba Nanoparticledispersions, Advanced materials **26** (38) (2014) 6653-6657.
- 18. Oliveira E. F., Silva L. C., Lavarda F.C. Modifying electronic properties of Icbathrough chemical substitutions for solar cell applications, Structural Chemistry **28** (2017) 1133-1140
- 19. Halls J., Walsh C., Greenham N. C., Marseglia E., Friend R. H., Moratti S., Holmes A. Efficient photodiodes from interpenetrating polymer networks, Nature **376** (6540) (1995) 98-500.
- 20. Yu G. J., Gao J. C., Hummelen F. Wudi, and A. J. Heeger Science 270 (1995) 1789.

- 21. Peet J., Kim J. Y., Coates N. E., Ma W. L., Moses D., Heeger A. J., Bazan G. C. Efficiency enhancement in low-bandgap polymer solar cells by Processing with alkane dithiols, Nature materials **6** (7) (2007) 497-500.
- 22. Lee J. K., Ma W. L., Brabec C. J., Yuen J., Moon J. S., Kim J. Y., Lee K., Bazan G. C., Heeger A. J. Processing additives for improved efficiency from bulk heterojunction solar cells, Journal of the American Chemical Society **130** (11) (2008) 3619-3623.
- 23. Loew N., Komatsu S., Akita H., Funayama K., Yuge T., Fujiwara T., Ihara M. TiO₂ as electron-extraction-layer in reverse type p3ht/icba organic solar cells, ECS Transactions **58** (45) (2014) 77.
- 24. Matavulj P., Islam M., 'Zivanovi C. S. Proceedings of the international Conferenceon numerical simulation of optoelectronic devices, (2017) 133-134.
- 25. Gopalan S. A., Gopalan A. I., Vinu A., Lee K. P., Kang S. W. A new optical lectrical integrated buffer layer design based on gold nanoparticles tethered thiol containing sulfonated polyaniline towards enhancement of solar cell performance, Solar Energy Materials and Solar Cells **174** (2018) 112-123.
- 26. Burgelman M., Nollet P., Degrave S. Modelling polycrystalline Semiconductorsolar cells, Thin solid films **361** (2000) 527-532.
- 27. Xu B., Sai-Anand G., Gopalan A. I., Qiao Q., Kang S. W. Improving hotovoltaic properties of p3ht: Ic60ba through the incorporation of small molecules, Polymers **0** (2) (2018) 121.
- 28. Nithya K., Sudheer K. Numerical modelling of non-fullerene organic solar Cellwith high dielectric constant itic-oe acceptor, Journal of Physics Communications **4** (2) (2020) 025012.
- 29. Heo S. W., Lee E. J., Seong K. W., Moon D. K. Enhanced stability in polymer solar cells by controlling the electrode work function via modification of indium tin oxide, Solar energy materials and solar cells **115** (2013) 123-128.
- 30. Loser S., Bruns C. J., Miyauchi H., Ortiz R. P., Facchetti A., Stupp S. I., Marks T. J. A naphthodithiophene-diketopyrrolopyrrole donor molecule for efficient solution- processed solar cells. Journal of the American Chemical Society **133** (21) (2011) 8142-8145.
- 31. Li G., Yao Y., Yang H., Shrotriya V., Yang G., Yang Y. "Solvent annealing" effect in polymer solar cells based on poly (3-hexylthiophene) and methanofullerenes, Advanced Functional Materials **17** (10) (2007) 1636-1644.
- 32. He Z., Liu F., Wang C., Chen J., He L., Nordlund D., Wu H., Russell T. P., Cao Y. Simultaneous spin-coating and solvent annealing: Manipulating the active layer morphology to a power conversion efficiency of 9.6 % in polymer solar cells, Materials Horizons 2 (6) (2015) 592-597.
- 33. Zhu X., Lu K., Xia B., Fang J., Zhao Y., Zhao T., Wei Z., Jiang L. Improving the performances of random copolymer based organic solar cells by adjusting the film features of active layers using mixed solvents, Polymers 8 (1) (2015) 4.
- 34. Lu L., Chen W., Xu T., Yu L. High-performance ternary blend polymer solar cells involving both energy transfer and hole relay processes, Nature communications **6** (1) (2015) 7327.

- 35. Stylianakis M. M., Konios D., Petridis C., Kakavelakis G., Stratakis E., Kymakis E. Ternary solution-processed organic solar cells incorporating 2D materials, 2D Materials **4** (4) (2017) 042005.
- 36. Ezealigo B. N., Nwanya A. C., Simo A., Osuji R. U., Bucher R., Maaza M., Ezema F. I. Optical and electrochemical capacitive properties of copper (i) iodide thin film deposited by silar method, Arabian Journal of Chemistry 12 (8) (2019) 5380-5391.
- 37. Liu J., Zhang Y., Liu C., Peng M., Yu A., Kou J., Liu W., Zhai J., Liu J. Piezo-phototronic effect enhanced uv photodetector based on cui/zno double-Shell grown on flexible copper microwire, Nanoscale research letters **11** (2016) 1-7.